

Transfer-printed multiple $\text{Ge}_{0.89}\text{Sn}_{0.11}$ membrane mid-infrared photodetectors

Cédric Lemieux-Leduc, Mahmoud R. M. Atalla, Simone Assali, Sebastian Koelling, Patrick Daoust, Lu Luo, Gérard Daligou, Julien Brodeur, Stéphane Kéna-Cohen, Yves-Alain Peter, and Oussama Moutanabbir*

*Department of Engineering Physics, Polytechnique Montréal, C.P. 6079, Succ.
Centre-Ville, Montréal, Québec, Canada H3C 3A7*

E-mail: oussama.moutanabbir@polymtl.ca

Abstract

Due to their narrow band gap and compatibility with silicon processing, germanium-tin ($\text{Ge}_{1-x}\text{Sn}_x$) alloys are a versatile platform for scalable integrated mid-infrared photonics. These semiconductors are typically grown on silicon wafers using Ge as an interlayer. However, the large lattice mismatch in this heteroepitaxy protocol leads to the build-up of compressive strain in the grown layers. This compressive strain limits the material quality and its thermal stability besides expanding the band gap, thereby increasing the Sn content needed to cover a broader range in the mid-infrared. Released $\text{Ge}_{1-x}\text{Sn}_x$ membranes provide an effective way to mitigate these harmful effects of the epitaxial strain and control the band gap energy while enabling the hybrid integration onto different substrates. With this perspective, herein strain-relaxed $\text{Ge}_{0.89}\text{Sn}_{0.11}$ membranes are fabricated and subsequently transfer-printed with metal contacts to create multiple photodetectors in a single transfer step. The resulting photodetectors exhibit an extended photodetection cutoff reaching a wavelength of $3.1\ \mu\text{m}$, coupled with

a significant reduction in the dark current of two orders of magnitude as compared to as-grown photoconductive devices. The latter yields a reduced cutoff of $2.8\ \mu\text{m}$ due to the inherent compressive strain. Furthermore, the impact of chemical treatment and annealing on the device performance was also investigated showing a further reduction in the dark current. The demonstrated transfer printing, along with the use of an adhesive layer, would allow the transfer of multiple GeSn membranes onto virtually any substrate. This approach paves the way for scalable fabrication of hybrid optoelectronic devices leveraging the tunable band gap of $\text{Ge}_{1-x}\text{Sn}_x$ in the mid-wave infrared range.

Introduction

The mid-wave infrared (MWIR, $2 - 8\ \mu\text{m}$) range is a highly strategic portion of the electromagnetic spectrum relevant to numerous applications in sensing, imaging, and free-space communication.¹⁻⁴ Current commercial platforms for MWIR detectors predominantly rely on III-V semiconductors such as InSb⁵ and type-II superlattices (T2SL)^{6,7} and II-VI compounds including HgCdTe (MCT).^{8,9} InSb and MCT detectors cover wavelengths up to $7\ \mu\text{m}$ and $12\ \mu\text{m}$, respectively, which enabled the development of MWIR imaging systems based on focal plane arrays (FPAs).^{10,11} While these technologies are mature, they remain costly, suffer from limited integration with silicon-based electronics, and are associated with a low bandwidth that is usually below 10 GHz for photodetectors with a cutoff wavelength above $2.3\ \mu\text{m}$.¹² Recently, germanium-tin ($\text{Ge}_{1-x}\text{Sn}_x$) alloys have emerged as alternate narrow-band gap materials for silicon-compatible MWIR optoelectronics.¹³ Indeed, this class of semiconductors covers a broad range of band gap energies by controlling the lattice strain and Sn content.¹³ $\text{Ge}_{1-x}\text{Sn}_x$ materials have been used in photodetectors operating at room temperature in the near-infrared (NIR) and MWIR,¹⁴⁻¹⁸ as well as for modulation based on the Franz-Keldysh effect.¹⁹ Additionally, $\text{Ge}_{1-x}\text{Sn}_x$ alloys also pave the way towards silicon-compatible light sources. Indeed, as the atomic content of Sn increases, the band gap at the Γ -valley diminishes faster than the one at the L-valley, leading to a transition to a di-

rect band gap when the Sn content exceeds 10 at.% Sn in a relaxed layer. This band gap directness has been exploited to implement silicon-integrated light emitting diodes^{20–22} and lasers.^{23–27} However, due to the low solubility of Sn in Ge (< 1 at.%) the growth of high-quality $\text{Ge}_{1-x}\text{Sn}_x$ layers with the minimal Sn composition required for MWIR applications poses challenges. Furthermore, the alloy suffers from a substantial lattice mismatch induced by the 14.7% difference between Ge and Sn atomic radii, resulting in compressively strained layers. This strain build-up leads to an increase in the band gap energy at the Γ -valley and impedes the Sn incorporation during growth, thus shrinking the wavelength range covered by the compressively strained devices.²⁸

Several approaches were investigated to alleviate these drawbacks,²⁹ including the growth of graded $\text{Ge}_{1-x}\text{Sn}_x$ buffers where the composition of Sn is gradually increased by controlling the temperature and precursors flow during growth.^{30–32} This method was found to be effective in partially relaxing the compressive strain in the top layer by allowing the misfit dislocations to glide in the initially grown $\text{Ge}_{1-x}\text{Sn}_x$ buffer layers. $\text{Ge}_{1-x}\text{Sn}_x$ nanowires offer an alternative method to relax strain at the facets without compromising the crystalline quality, enabling nanoscale optoelectronic devices with promising performance.^{33–38} For applications requiring larger active material areas, strain-relaxed membranes emerge as a promising solution to mitigate the harmful effects of compressive strain.^{39,40} Material properties that are practically unattainable by conventional growth or wafer bonding techniques can be achieved through the transfer of membranes onto a wide variety of substrates using transfer printing.^{41,42} While group-IV^{43,44} and III-V⁴⁵ semiconductor membranes have been introduced for broadband photodetection and light emission, their operational range does not cover the MWIR. Although progress has been made in membranes based on InAs/InAsSb T2SLs⁴⁶ and ultrathin MCT layers,⁴⁷ $\text{Ge}_{1-x}\text{Sn}_x$ alloys provide a solution to implement transferable group-IV MWIR membrane-based photodetectors.^{48–52} The fabrication of $\text{Ge}_{0.83}\text{Sn}_{0.17}$ membrane photodetectors resulted in an impressive increase in the detection cutoff from 3.5 μm to 4.6 μm while maintaining operation at room-temperature.⁵⁰ Moreover, $\text{Ge}_{1-x}\text{Sn}_x$ membranes

provide a reduced dark current as the conductive Ge and Si layers underneath are removed, which helps in improving the power dissipation and allows the use of a higher bias voltage. However, these membranes suffered from a structural bowing that reduces their adherence to the host substrate after using transfer printing. Alleviating these limitations requires revisiting the growth process to minimize the compressive strain in addition to introducing an adhesive layer⁵³ and reducing the number of post-processing steps by adding transferable contacts.⁵⁴

Herein, to demonstrate the mass-transfer of GeSn membranes, we fabricated $\text{Ge}_{0.89}\text{Sn}_{0.11}$ membrane metal-semiconductor-metal (MSM) photodetectors that operate at room temperature with a cutoff of $3.1\ \mu\text{m}$ and a reduced dark current. The growth of a single $\text{Ge}_{0.89}\text{Sn}_{0.11}$ layer led to membranes with a reduced bowing and an initial compressive strain of -0.6% before the membrane release. The reduced bowing helps in transferring membranes efficiently as an array at a high yield while the relaxation of the residual compressive strain aids extend the photodetection cutoff. To streamline the processing steps, transferable contacts are initially exfoliated and affixed to an elastomeric stamp before the transfer printing step, ensuring their attachment to the membranes. This results in an array of contacted devices upon completion of the transfer process. SU-8, which is used as an adhesive and an insulating layer, is spin-coated on the host substrate before transfer printing. Subsequently, the performance of the membrane devices is systematically analyzed and compared to their as-grown counterparts, followed by the discussion of the influence of chemical treatment and annealing on device characteristics.

Results and discussion

Growth and characterization of GeSn epilayers

The $\text{Ge}_{0.89}\text{Sn}_{0.11}$ alloy growth was carried out in a low-pressure chemical vapor deposition (CVD) reactor on a 4-inch Si (100) wafer. First, a $1.02\ \mu\text{m}$ -thick Ge virtual substrate (Ge-

VS) was grown using 10% monogermane (GeH_4) and a continuous flow of pure hydrogen following a two-temperature growth protocol at 460°C and 600°C . In addition to reducing the lattice mismatch between the Si substrate and GeSn, Ge-VS also acts as a sacrificial layer, facilitating the GeSn membranes underetching and release.

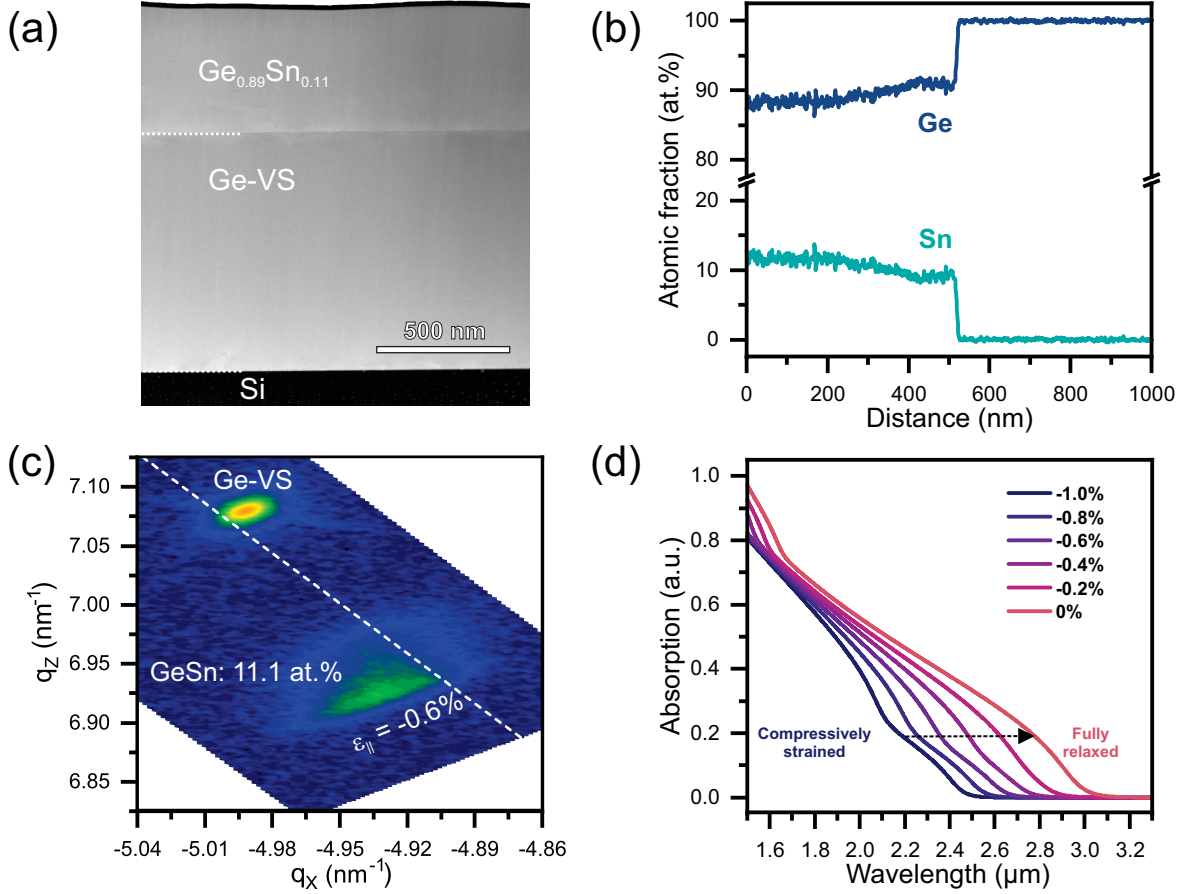


Figure 1: Properties of the as-grown $\text{Ge}_{0.89}\text{Sn}_{0.11}$ alloy. (a) Cross-sectional TEM image of the layer stack. (b) EDX Ge and Sn profiles in the grown layer, starting from the top of the GeSn layer. (c) XRD-RSM around the asymmetrical (224) reflection peak, providing the composition and strain in the as-grown $\text{Ge}_{0.89}\text{Sn}_{0.11}$ layer. (d) 8-band $k\cdot p$ calculations of the room-temperature absorption of the $\text{Ge}_{0.89}\text{Sn}_{0.11}$ layer by varying the in-plane strain from compressive strain (-1%) to full relaxation (0%).

Subsequently, a $\text{Ge}_{0.89}\text{Sn}_{0.11}$ film was grown on Ge-VS at 320°C using GeH_4 and SnCl_4 precursors. The microstructure of the as-grown material was assessed using cross-sectional transmission electron microscopy (TEM), as displayed in Fig. 1(a). Notably, a high density of threading dislocations and defects is localized at the Ge-VS/Si and $\text{Ge}_{0.89}\text{Sn}_{0.11}$ /Ge-VS

interfaces, indicative of misfit dislocation gliding^{28,30} while the top of the $\text{Ge}_{0.89}\text{Sn}_{0.11}$ layer is relatively defect-free. To obtain a more detailed understanding of the alloy’s elemental composition, energy-dispersive X-ray spectroscopy (EDX) is employed. Fig. 1(b) exhibits the measured Sn and Ge composition profiles, revealing the approximate atomic fraction of Ge and Sn across the $\text{Ge}_{1-x}\text{Sn}_x$ layer. The layer thickness is estimated to be approximately 520 nm and the Sn composition starts at 9% as it increases towards 12% from the bottom to the top of the $\text{Ge}_{1-x}\text{Sn}_x$ layer respectively. The background noise coming from the surrounding elements during the EDX measurements was subtracted to avoid an overestimation of the Sn content.

For a comprehensive analysis of the composition and strain in the sample, X-ray diffraction reciprocal space mapping (XRD-RSM) is performed around the asymmetrical (-2-24) reflection peak, as depicted in Fig. 1(c). The map reveals peaks related to the Ge-VS and the GeSn layers. Using the GeSn peak, a composition of 11.1% Sn and an in-plane biaxial compressive strain ε_{\parallel} of -0.6% are extracted. This composition value is within the range observed in the Sn profile from EDX in Fig. 1(b) and will be used throughout this study.

Fig. 1(d) depicts calculations of the absorption spectrum based on the semi-empirical 8-band $k \cdot p$ theory⁵⁵ as the compressive strain is varied from -1% to 0% at 300 K. Bowing parameters are implemented in the model to reduce the relative error in the estimation of the band gap at the Γ and L symmetry points using Vegard’s law. Strain-independent values of 2.85 eV at the Γ point and 1.23 eV at the L point were used for the bowing parameters in these calculations. Expectedly, a remarkable increase in the absorption wavelength cutoff is observed as the band energy shrinks due to strain relaxation.

GeSn membrane fabrication and transfer printing

The fabrication of $\text{Ge}_{0.89}\text{Sn}_{0.11}$ membranes starts with a standard photolithography of the as-grown sample to pattern an array of $20 \mu\text{m} \times 20 \mu\text{m}$ squares with a pitch of $200 \mu\text{m} \times 400 \mu\text{m}$, as shown in Fig. 2(a). These patterns are subsequently transferred onto the $\text{Ge}_{0.89}\text{Sn}_{0.11}$ sample by wet etching of GeSn and Ge-VS layers using a mixture of ceric ammo-

nium nitrate and nitric acid. The wet etching process induces an undercut of approximately $1\ \mu\text{m}$ with tapered sidewalls, reaching a depth of $1.4\ \mu\text{m}$. By selectively etching the Ge-VS, membranes are formed and fully released from the Si substrate using a CF_4 -based plasma dry etch. The selectivity in etching Ge-VS rather than $\text{Ge}_{1-x}\text{Sn}_x$ arises from the reaction of fluoride-based radicals with Sn at the exposed surface of $\text{Ge}_{1-x}\text{Sn}_x$. This reaction produces a thin, non-volatile SnF_y layer, effectively shielding the layer from further etching and ensuring a high selectivity.⁵⁶ Images of a single released $\text{Ge}_{0.89}\text{Sn}_{0.11}$ membrane are shown in Fig. 2(b) using optical microscopy (left) and scanning electron microscope (SEM) (right). A slight downward bowing can be observed in the SEM image, indicating either remaining traces of the Ge-VS layer at the center of the membrane or a partial etching of the edge compared to the outer contour of the membrane.

To assess the impact of the underetching process on strain relaxation, room-temperature Raman spectroscopy measurements were conducted on both as-grown and membrane samples. The acquisition of the Raman spectra shown in Fig. 2(c) was carried out using a 633 nm excitation laser and a $100\times$ microscope objective lens. The Ge–Ge longitudinal (LO) phonon Raman peak is located around $300\ \text{cm}^{-1}$ in pure Ge and it can either red-shift as the Sn concentration increases or blue-shift as the compressive strain increases.⁵⁷ The peak position shifts from $294.3\ \text{cm}^{-1}$ in the as-grown alloy to $292.1\ \text{cm}^{-1}$ in the membrane, which indicates a relaxation of the compressive strain. Here, a fit with an exponentially modified Gaussian function was performed to extract the central frequency of the asymmetrical Raman peak.⁵⁷ It is important to note that the released membranes may be subject to local strain fluctuations,⁵⁰ which should impact the optical properties as the band structure is locally modified. Room-temperature photoluminescence (PL) analysis was carried out on the investigated samples using an 808 nm excitation laser. The PL peak serves as an approximate indicator of the band gap energy and the absorption range. A $40\times$ microscope reflective objective lens with a $7\ \mu\text{m}$ spot size was used to focus the light on a single $\text{Ge}_{0.89}\text{Sn}_{0.11}$ membrane. The spectrum of the as-grown sample depicts a single peak centered

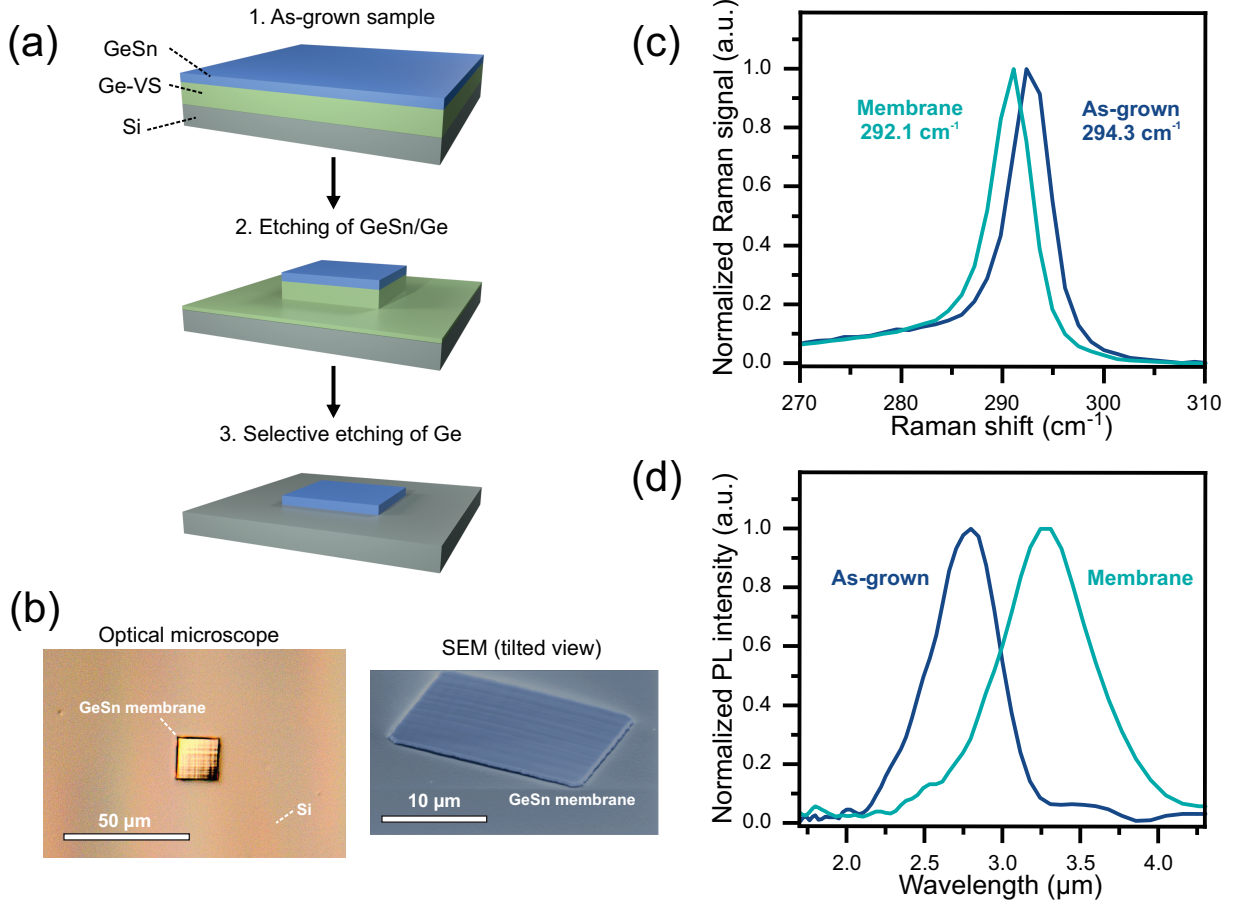


Figure 2: Membrane fabrication. (a) Illustration of the $\text{Ge}_{0.89}\text{Sn}_{0.11}$ membrane fabrication steps. (b) Optical microscope image and SEM micrograph of a released $\text{Ge}_{0.89}\text{Sn}_{0.11}$ membrane. (c) Raman spectroscopy measurements of the as-grown and the membrane samples with the position of the Ge–Ge longitudinal phonon Raman peak indicated. (d) Photoluminescence spectra of the as-grown and membrane samples acquired at room temperature.

at $2.8\ \mu\text{m}$ while the membrane shows a single peak at $3.3\ \mu\text{m}$. This redshift of the PL peak indicates a reduction of the band gap energy in the released membrane compared to the as-grown sample, which is in qualitative agreement with the $k \cdot p$ calculations (Fig. 1(d)), showing that the band gap is expected to shrink as the compressive strain is relaxed.

The fabrication of $\text{Ge}_{0.89}\text{Sn}_{0.11}$ membrane photodetectors was carried out using a transfer printing technique,^{41,42} as illustrated in Fig. 3(a). This technique utilizes a setup equipped with a microscope and mechanical stages within a glovebox with a nitrogen environment. An elastomeric PDMS stamp, sized roughly $2\ \text{mm} \times 2\ \text{mm}$, enables the simultaneous pick up of

multiple membranes. To create photoconductive detectors, metal contacts are first detached from a separate substrate using mechanical exfoliation. These contacts are then affixed to a PDMS stamp before picking up the membranes. In this approach, pre-processed exfoliated contacts are utilized since the adhesive layer (SU-8) can be easily removed during a metal lift-off process. This technique is versatile and can be employed with various substrates without subjecting them to potentially damaging process conditions. A transferable array of metal contacts with a 5 μm contact separation gap is patterned in a photoresist layer coated on a separate SiO_2/Si substrate using photolithography. Subsequently, a 200 nm-thick Au layer is deposited via electron beam evaporation followed by a lift-off process (Fig. 3(a), step 1.1). The substrate with the Au contacts is then coated with a polycarbonate layer (Fig. 3(a), step 1.2) to facilitate the mechanical exfoliation of the contacts (Fig. 3(a), step 1.3) and enhance their adherence to the PDMS stamp (Fig. 3(a), step 1.4). The donor substrate, which has the released $\text{Ge}_{0.89}\text{Sn}_{0.11}$ membranes, is positioned beneath the PDMS stamp with alignment marks aiding in aligning the membranes between the contact pads (Fig. 3(a), step 2.1). The membranes are then picked up by applying pressure on the sample using the PDMS stamp with the exfoliated contacts (Fig. 3(a), step 2.2). Subsequently, the PDMS stamp is lifted back to its original position to complete the membrane pick up (Fig. 3(a), step 2.3). Afterward, the Si receiver substrate coated with an SU-8 layer is placed beneath the PDMS stamp containing the contacted devices (Fig. 3(a), step 3.1). To transfer the contacted devices, pressure is applied using the PDMS stamp onto the receiver substrate (Fig. 3(a), step 3.2) and the temperature is increased to 200 °C to melt the polycarbonate film, facilitating the separation of devices from the PDMS stamp (Fig. 3(a), step 3.3). The transfer process is finalized by dissolving the polycarbonate film in dichloromethane for 30 s (Fig. 3(a), step 3.4). To enhance the quality of the Au contacts, the devices undergo annealing at 280 °C for 30 min.

Fig. 3(b) presents a microscope image of transferred devices with close-up views from SEM micrographs of representative devices. A noticeable misalignment of contacts with

membranes is observed, attributable to both the limited alignment accuracy of the setup and the displacement of the released GeSn membranes from their initial array position during underetch release. The latter can potentially be resolved by an improved design of the membranes or by adding mechanical anchors, which can hold membranes after their complete underetching and can be easily broken during the pick up step.⁵⁸

Device characterization

Electrical characterization of the $\text{Ge}_{0.89}\text{Sn}_{0.11}$ photoconductive (PC) devices was conducted using a Keithley 4200A semiconductor parameter analyzer to assess their performance. The transferred membrane devices are compared to as-grown $\text{Ge}_{0.89}\text{Sn}_{0.11}$ PC devices to highlight the advantages of strain relaxation and transfer onto a dielectric-capped substrate. Dark current as a function of voltage, as shown in Fig. 4(a), is systematically measured from -4 V to 4 V for both the as-grown and the membrane samples. A pronounced reduction by two orders of magnitude in the dark current is observed in the membrane device compared to its as-grown counterpart. The Schottky behavior observed in the dark current curve of the membrane device is most likely due to the passivation resulting from the underetching of Ge using a CF_4 plasma, leading to a suppression of the number of surface states through the formation of Ge-F covalent bonds and subsequent alleviation of Fermi level pinning.⁵⁹

The spectral responsivity for both as-grown and membrane devices is presented in Fig. 4(b). The acquisition of the responsivity spectra was carried out using a Fourier-transform infrared (FTIR) spectrometer (Bruker Vertex 70), with a calibrated tungsten lamp serving as a MWIR source. The MWIR light is focused onto the device using a $40\times$ microscope reflective objective lens. The photocurrent was measured under a bias of 1 V and using a lock-in technique synchronized to an FTIR step scan to acquire the spectral intensity response of the measured PC devices. The spectral responsivity can then be determined from the measured intensity spectra using a calibrated InSb photodetector. A responsivity of 0.3 mA/W is measured at $1.55\ \mu\text{m}$ for the membrane device, and the cutoff wavelength is increased from $2.8\ \mu\text{m}$ to $3.1\ \mu\text{m}$ relative to the as-grown device. The measured wavelength

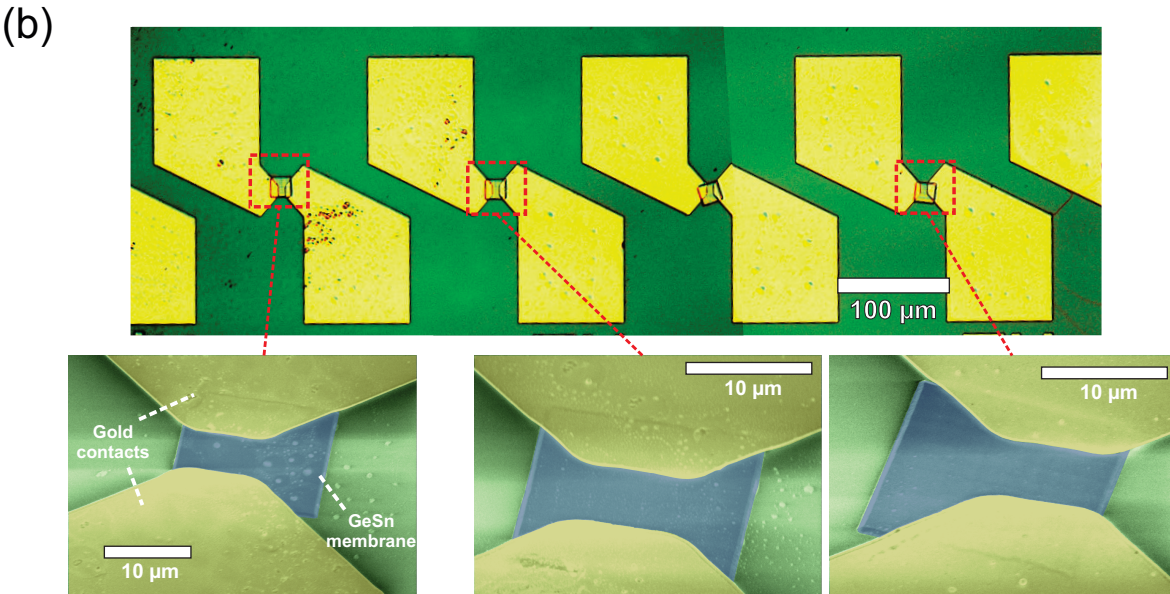
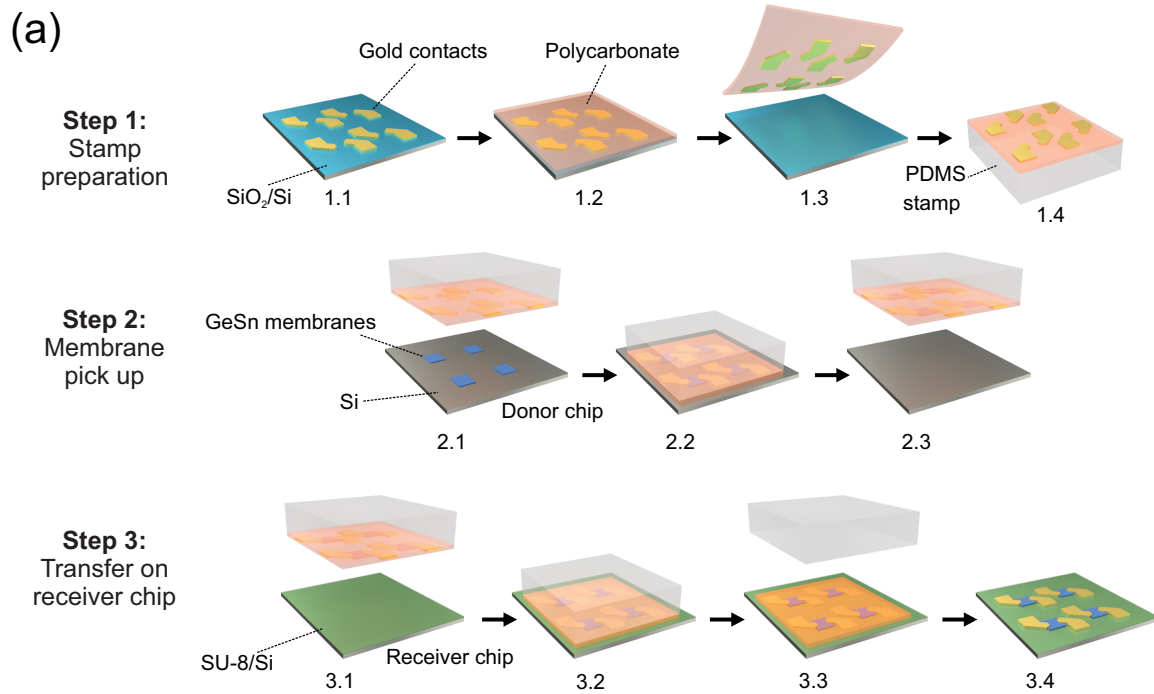


Figure 3: Membrane photodetector fabrication via transfer printing. (a) Transfer printing steps. (b) Optical microscope image of multiple membrane devices (top) along with SEM images of selected devices (bottom).

cutoff values are similar to the absorption cutoff values computed using 8-band kp (Fig. 1(d)) at their respective strain values within less than $\sim 4\%$ uncertainty. The latter is strongly dependent on the bowing parameters used in the model.⁵⁵

The transient response of the membrane photodetector is investigated under a bias of 1

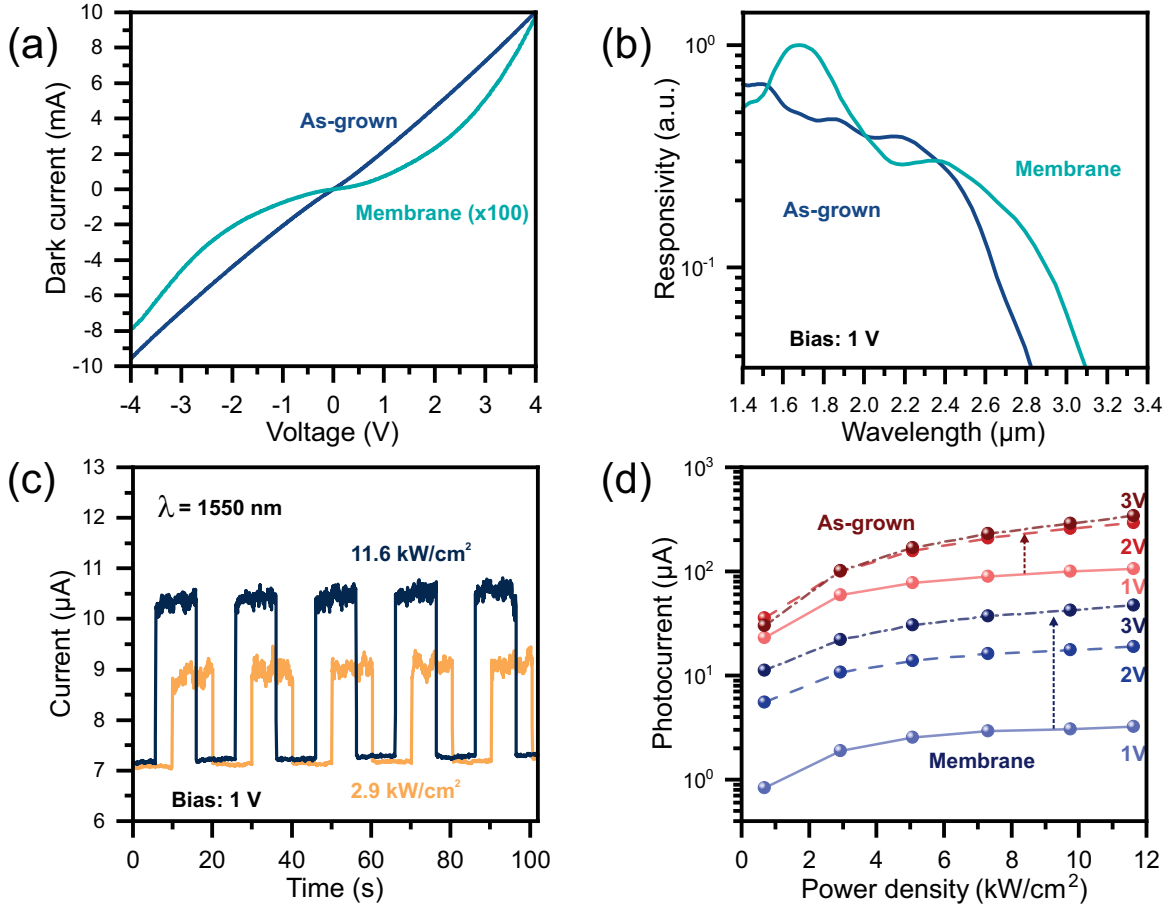


Figure 4: Photoconductive device characterization. (a) Dark current of the contacted membrane and as-grown samples as a function of voltage. (b) Spectral responsivity of the membrane and as-grown devices under a bias of 1 V. (c) Time-dependent photocurrent response of a membrane device under a bias of 1 V and illuminated under different power densities using a $1.55 \mu\text{m}$ laser. (d) Photocurrent as a function of power density and of applied bias.

V using a 1550 nm laser, as shown in Fig. 4(c). A distinctive increase in the total current is observed as the illumination is varied over several cycles at a fixed power density. As the power density increases from $2.9 \text{ kW}/\text{cm}^2$ to $11.6 \text{ kW}/\text{cm}^2$, the collected photocurrent increases from $1.9 \mu\text{A}$ to $3.2 \mu\text{A}$. Fig. 4(d) presents the photocurrent measured as a function of power density for both as-grown and membrane samples at biases ranging from 1 V to 3 V. A notable increase in the photocurrent is noted with rising incident light power density and applied bias. Specifically, the $\text{Ge}_{0.89}\text{Sn}_{0.11}$ membrane photodetector exhibits an increase in responsivity at 1550 nm from $0.3 \text{ mA}/\text{W}$ to $8.8 \text{ mA}/\text{W}$ as the bias is increased from 1 V

to 3 V. In contrast, the as-grown sample shows an increase from 13.8 mA/W to 89 mA/W over the same bias range.

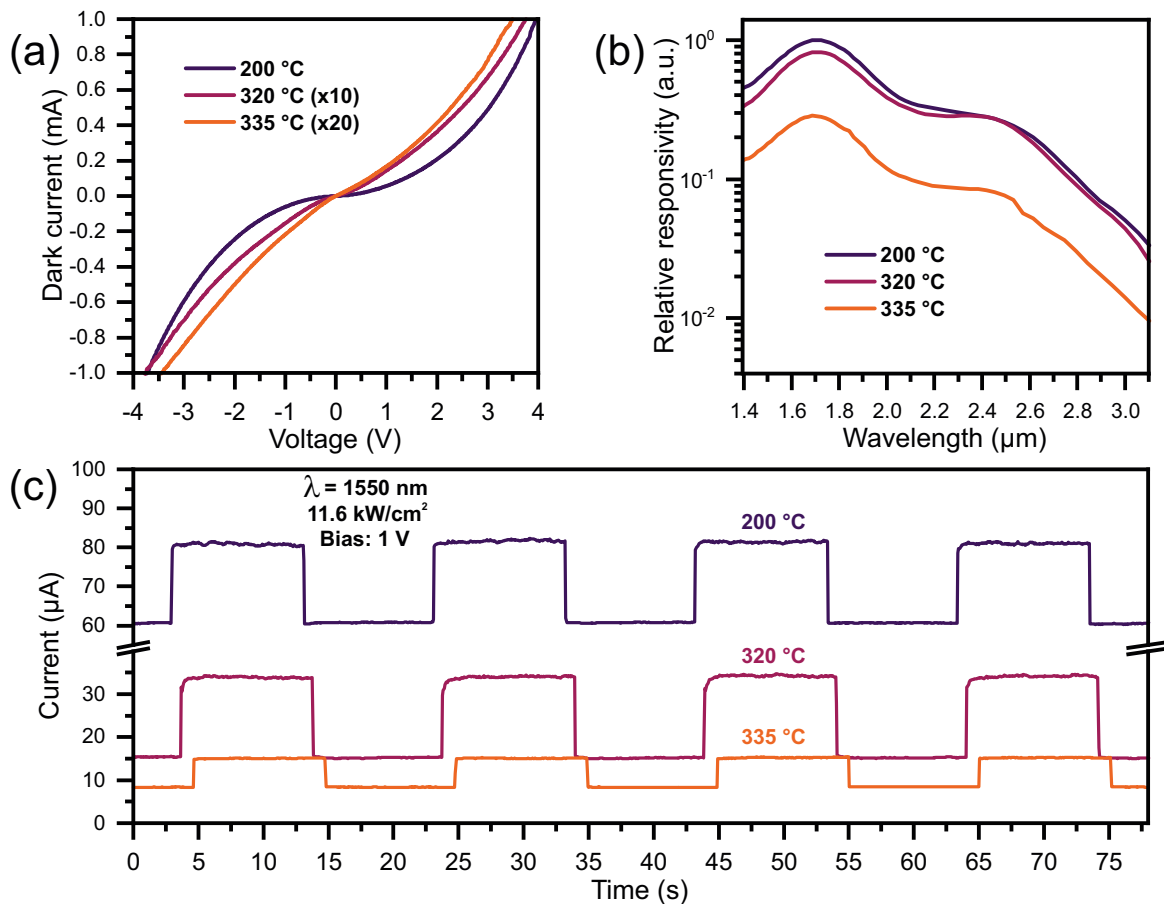


Figure 5: Device characterization after chemical treatment and annealing at different temperatures. (a) Dark current as a function of voltage. (b) Spectral responsivity normalized to the measurement made with the annealing at 200 °C. (c) Time-dependent photocurrent response under a bias of 1 V and illuminated by a 1.55 μm laser at a power density of 11.6 kW/cm².

The responsivity of the membrane devices can potentially be improved by removing the residual non-volatile species from the release step using cleaning solutions⁵⁶ and by annealing the contacts.⁶⁰ It is expected that Sn should start segregating in Ge_{0.89}Sn_{0.11} at an annealing temperature close to the growth temperature,⁶¹ which is an additional constraint in post-growth processing. In this regard, new devices were fabricated to investigate the influence of surface treatments on the membranes and the annealing of the contacts. To isolate

these effects, the process flow is modified to first transfer the membranes to the host chip without transferable contacts. Subsequently, the chip undergoes immersion in a mixture of water and hydrochloric acid (4 H₂O : 1 HCl) for 10 s, followed by rinsing in water. The exfoliated contacts are then transferred in a second transfer printing step thereafter. As the polycarbonate film is melted at 200 °C, membranes and contacts are initially annealed at this temperature for 10 min. The dark current and the responsivity are measured before and after the device annealing at 320 °C and 335 °C close to the growth temperature.

The obtained device exhibits a responsivity of 3.1 mA/W at 1.55 μm, representing a tenfold increase in comparison to untreated devices. This enhancement may be attributed to the partial removal of residual by-products that could have created a barrier for the carriers. As the annealing temperature increases, the magnitude of the dark current decreases as depicted in Fig. 5(a). The dark current decreases by a factor of 10 after annealing at 320 °C and by an additional factor of 2 after annealing at 335 °C while gradually leaning towards an Ohmic behavior. Although the spectral responsivity maintains a consistent wavelength range at different annealing temperatures, a reduction in the responsivity is observed when compared to the initial annealing carried out at 200 °C, as shown in Fig. 5(b). Specifically, it diminishes to 2.6 mA/W and 0.9 mA/W after annealing at 320 °C and 335 °C, respectively.

The time-dependent response of the device under a 1 V bias and illumination by a 1.55 μm laser at a power density of 11.6 kW/cm² is presented in Fig. 5(c) for different annealing temperatures. Remarkably, a reduction in both dark current and photocurrent is observed with increasing annealing temperatures. This reduction in dark current is mainly attributed to an enhancement in the crystalline quality of Ge_{0.89}Sn_{0.11} through annealing, likely reducing vacancy-like defects capable of trapping charge carriers.⁶² However, an increase in contact resistivity may also contribute to the reduction with rising annealing temperatures as less photocurrent is being collected. These factors appear to be competing, highlighting the need for defect removal in the microstructure with a minimal impact on contact resistivity.

Conclusion

In summary, $\text{Ge}_{0.89}\text{Sn}_{0.11}$ membrane photodetectors were developed and characterized showing room-temperature operation in the mid-infrared range. The control of Sn content and lattice strain throughout the epitaxial growth yielded highly relaxed alloys leading to released membranes without any significant structural bowing, thus facilitating the large-scale transfer of membrane detector arrays. Indeed, the fabrication process based on transfer printing was improved by using an SU-8 adhesive layer and transferable gold contacts. These improvements enabled the transfer of multiple membrane-based photoconductive devices in a single transfer printing step. Furthermore, the effects of annealing and chemical treatment on the photodetectors were explored to identify avenues to improve the device's performance. During the release, the membranes were subjected to an additional relaxation of the residual strain inducing an extension of the cutoff wavelength from $2.8\ \mu\text{m}$ to $3.1\ \mu\text{m}$. Moreover, the transferred detectors were found to exhibit two orders of magnitude reduction in the dark current as compared to detectors made of as-grown layers. Our findings not only underscore the potential of $\text{Ge}_{1-x}\text{Sn}_x$ membranes as a robust group IV platform for MWIR photodetection and sensing but also emphasize the ongoing progress in their practical implementation. A platform based on group IV semiconductors benefits from compatibility with silicon, which is vital for the development of large-scale MWIR components.

Acknowledgments

The authors thank J. Bouchard for the technical support with the CVD system and the Microfabrication Laboratory (LMF) for the support with the microfabrication steps. O.M. acknowledges support from NSERC Canada (Discovery, SPG, and CRD Grants), Canada Research Chairs, Canada Foundation for Innovation, Mitacs, PRIMA Québec, Defence Canada (Innovation for Defence Excellence and Security, IDEaS), the European Union's Horizon Europe research and innovation program under grant agreement No 101070700 (MIRAQLS),

the US Army Research Office Grant No. W911NF-22-1-0277, and the Air Force Office of Scientific Research Grant No. FA9550-23-1-0763. C.L.-L. acknowledges financial support from NSERC (CGS D) and Fonds de recherche du Québec: Nature and Technologies (FRQNT, doctoral scholarship).

References

- (1) Lin, H.; Luo, Z.; Gu, T.; Kimerling, L. C.; Wada, K.; Agarwal, A.; Hu, J. Mid-infrared integrated photonics on silicon: a perspective. *Nanophotonics* **2018**, *7*, 393–420.
- (2) Popa, D.; Udrea, F. Towards integrated mid-infrared gas sensors. *Sensors* **2019**, *19*, 2076.
- (3) Razeghi, M.; Nguyen, B.-M. Advances in mid-infrared detection and imaging: a key issues review. *Reports on Progress in Physics* **2014**, *77*, 082401.
- (4) Sieger, M.; Mizaikoff, B. Toward on-chip mid-infrared sensors. *Analytical Chemistry* **2016**, *88*, 5562–5573.
- (5) Alimi, Y.; Pusino, V.; Steer, M. J.; Cumming, D. R. S. InSb avalanche photodiodes on GaAs substrates for mid-infrared detection. *IEEE Transactions on Electron Devices* **2019**, *67*, 179–184.
- (6) Müller, R.; Haertelt, M.; Niemasz, J.; Schwarz, K.; Daumer, V.; Flores, Y. V.; Ostendorf, R.; Rehm, R. Thermoelectrically-cooled InAs/GaSb Type-II superlattice detectors as an alternative to HgCdTe in a real-time mid-infrared backscattering spectroscopy system. *Micromachines* **2020**, *11*, 1124.
- (7) Alshahrani, D. O.; Kesaria, M.; Anyebe, E. A.; Srivastava, V.; Huffaker, D. L. Emerging Type-II Superlattices of InAs/InAsSb and InAs/GaSb for Mid-Wavelength Infrared Photodetectors. *Advanced Photonics Research* **2022**, *3*, 2100094.

- (8) Rogalski, A. In *Mid-infrared Optoelectronics*; Tournié, E., Cerutti, L., Eds.; Woodhead Publishing Series in Electronic and Optical Materials; Woodhead Publishing, 2020; pp 235–335.
- (9) Li, F.; Deng, J.; Zhou, J.; Chu, Z.; Yu, Y.; Dai, X.; Guo, H.; Chen, L.; Guo, S.; Lan, M.; Chen, X. HgCdTe mid-Infrared photo response enhanced by monolithically integrated meta-lenses. *Scientific Reports* **2020**, *10*, 6372.
- (10) Pusino, V.; Xie, C.; Khalid, A.; Steer, M. J.; Sorel, M.; Thayne, I. G.; Cumming, D. R. S. InSb photodiodes for monolithic active focal plane arrays on GaAs substrates. *IEEE Transactions on Electron Devices* **2016**, *63*, 3135–3142.
- (11) Lei, W.; Antoszewski, J.; Faraone, L. Progress, challenges, and opportunities for HgCdTe infrared materials and detectors. *Applied Physics Reviews* **2015**, *2*, 041303.
- (12) Chen, B.; Chen, Y.; Deng, Z. Recent advances in high speed photodetectors for eSWIR/MWIR/LWIR applications. *Photonics* **2021**, *8*, 14.
- (13) Moutanabbir, O.; Assali, S.; Gong, X.; O'Reilly, E.; Broderick, C. A.; Marzban, B.; Witzens, J.; Du, W.; Yu, S.-Q.; Chelnokov, A.; Buca, D.; Nam, D. Monolithic infrared silicon photonics: The rise of (Si)GeSn semiconductors. *Applied Physics Letters* **2021**, *118*, 110502.
- (14) Tran, H. et al. Si-based GeSn photodetectors toward mid-infrared imaging applications. *ACS Photonics* **2019**, *6*, 2807–2815.
- (15) Li, X.; Peng, L.; Liu, Z.; Zhou, Z.; Zheng, J.; Xue, C.; Zuo, Y.; Chen, B.; Cheng, B. 30 GHz GeSn photodetector on SOI substrate for 2 μm wavelength application. *Photonics Research* **2021**, *9*, 494–500.
- (16) Talamas Simola, E.; Kiyek, V.; Ballabio, A.; Schlykow, V.; Frigerio, J.; Zucchetti, C.; De Iacovo, A.; Colace, L.; Yamamoto, Y.; Capellini, G.; Grützmacher, D.; Buca, D.;

- Isella, G. CMOS-compatible bias-tunable dual-band detector based on GeSn/Ge/Si coupled photodiodes. *ACS Photonics* **2021**, *8*, 2166–2173.
- (17) Atalla, M. R. M.; Assali, S.; Koelling, S.; Attiaoui, A.; Moutanabbir, O. High-bandwidth extended-SWIR GeSn photodetectors on silicon achieving ultrafast broadband spectroscopic response. *ACS Photonics* **2022**, *9*, 1425–1433.
- (18) Liu, X.; Zheng, J.; Niu, C.; Liu, T.; Huang, Q.; Li, M.; Zhang, D.; Pang, Y.; Liu, Z.; Zuo, Y.; Cheng, B. Sn content gradient GeSn with strain controlled for high performance GeSn mid-infrared photodetectors. *Photonics Research* **2022**, *10*, 1567–1574.
- (19) Hsieh, Y.-D.; Lin, J.-H.; Soref, R.; Sun, G.; Cheng, H.-H.; Chang, G.-E. Electro-absorption modulation in GeSn alloys for wide-spectrum mid-infrared applications. *Communications Materials* **2021**, *2*, 40.
- (20) Stange, D.; von den Driesch, N.; Rainko, D.; Roesgaard, S.; Povstugar, I.; Hartmann, J.-M.; Stoica, T.; Ikonic, Z.; Mantl, S.; Grützmacher, D.; Buca, D. Short-wave infrared LEDs from GeSn/SiGeSn multiple quantum wells. *Optica* **2017**, *4*, 185–188.
- (21) Chang, C.-Y.; Yeh, P.-L.; Jheng, Y.-T.; Hsu, L.-Y.; Lee, K.-C.; Li, H.; Cheng, H. H.; Chang, G.-E. Mid-infrared resonant light emission from GeSn resonant-cavity surface-emitting LEDs with a lateral pin structure. *Photonics Research* **2022**, *10*, 2278–2286.
- (22) Atalla, M. R.; Kim, Y.; Assali, S.; Burt, D.; Nam, D.; Moutanabbir, O. Extended-SWIR GeSn LEDs with Reduced Footprint and Efficient Operation Power. *ACS Photonics* **2023**, *10*, 1649–1653.
- (23) Chrétien, J. et al. GeSn lasers covering a wide wavelength range thanks to uniaxial tensile strain. *ACS Photonics* **2019**, *6*, 2462–2469.
- (24) Kim, Y.; Assali, S.; Burt, D.; Jung, Y.; Joo, H.-J.; Chen, M.; Ikonic, Z.; Moutanab-

- bir, O.; Nam, D. Enhanced GeSn microdisk lasers directly released on Si. *Advanced Optical Materials* **2022**, *10*, 2101213.
- (25) Zhou, Y. et al. Electrically injected GeSn lasers with peak wavelength up to 2.7 μm . *Photonics Research* **2022**, *10*, 222–229.
- (26) Chrétien, J.; Thai, Q. M.; Frauenrath, M.; Casiez, L.; Chelnokov, A.; Reboud, V.; Hartmann, J.-M.; El Kurdi, M.; Pauc, N.; Calvo, V. Room temperature optically pumped GeSn microdisk lasers. *Applied Physics Letters* **2022**, *120*, 051107.
- (27) Buca, D.; Bjelajac, A.; Spirito, D.; Concepción, O.; Gromovyi, M.; Sakat, E.; Lafosse, X.; Ferlazzo, L.; von den Driesch, N.; Ikonik, Z.; Grützmacher, D.; Capellini, G.; El Kurdi, M. Room temperature lasing in GeSn microdisks enabled by strain engineering. *Advanced Optical Materials* **2022**, *10*, 2201024.
- (28) Assali, S.; Nicolas, J.; Moutanabbir, O. Enhanced Sn incorporation in GeSn epitaxial semiconductors via strain relaxation. *Journal of Applied Physics* **2019**, *125*, 025304.
- (29) Nawwar, M. A.; Ghazala, M. S. A.; El-Deen, L. M. S.; Kashyout, A. E.-h. B. Impact of strain engineering and Sn content on GeSn heterostructured nanomaterials for nanoelectronics and photonic devices. *RSC Advances* **2022**, *12*, 24518–24554.
- (30) Aubin, J.; Hartmann, J.-M.; Gassenq, A.; Rouviere, J.-L.; Robin, E.; Delaye, V.; Cooper, D.; Mollard, N.; Reboud, V.; Calvo, V. Growth and structural properties of step-graded, high Sn content GeSn layers on Ge. *Semiconductor Science and Technology* **2017**, *32*, 094006.
- (31) Dou, W.; Benamara, M.; Mosleh, A.; Margetis, J.; Grant, P.; Zhou, Y.; Al-Kabi, S.; Du, W.; Tolle, J.; Li, B.; Mortazavi, M.; Yu, S.-Q. Investigation of GeSn strain relaxation and spontaneous composition gradient for low-defect and high-Sn alloy growth. *Scientific Reports* **2018**, *8*, 5640.

- (32) Assali, S.; Nicolas, J.; Mukherjee, S.; Dijkstra, A.; Moutanabbir, O. Atomically uniform Sn-rich GeSn semiconductors with 3.0–3.5 μm room-temperature optical emission. *Applied Physics Letters* **2018**, *112*, 251903.
- (33) Meng, A. C.; Fenrich, C. S.; Braun, M. R.; McVittie, J. P.; Marshall, A. F.; Harris, J. S.; McIntyre, P. C. Core-shell germanium/germanium–tin nanowires exhibiting room-temperature direct-and indirect-gap photoluminescence. *Nano Letters* **2016**, *16*, 7521–7529.
- (34) Assali, S.; Dijkstra, A.; Li, A.; Kölling, S.; Verheijen, M. A.; Gagliano, L.; von Den Driesch, N.; Buca, D.; Koenraad, P. M.; Haverkort, J. E. M.; Bakkers, E. P. A. M. Growth and optical properties of direct band gap Ge/Ge_{0.87}Sn_{0.13} core/shell nanowire arrays. *Nano Letters* **2017**, *17*, 1538–1544.
- (35) Luo, L.; Assali, S.; Atalla, M. R.; Koelling, S.; Attiaoui, A.; Daligou, G.; Martí, S.; Arbiol, J.; Moutanabbir, O. Extended-SWIR photodetection in all-group IV core/shell nanowires. *ACS Photonics* **2022**, *9*, 914–921.
- (36) Assali, S.; Albani, M.; Bergamaschini, R.; Verheijen, M. A.; Li, A.; Kölling, S.; Gagliano, L.; Bakkers, E. P. A. M.; Miglio, L. Strain engineering in Ge/GeSn core/shell nanowires. *Applied Physics Letters* **2019**, *115*, 113102.
- (37) Kim, Y.; Assali, S.; Joo, H.-J.; Koelling, S.; Chen, M.; Luo, L.; Shi, X.; Burt, D.; Ikonic, Z.; Nam, D.; Moutanabbir, O. Short-wave infrared cavity resonances in a single GeSn nanowire. *Nature Communications* **2023**, *14*, 4393.
- (38) Luo, L.; Atalla, M. R.; Assali, S.; Koelling, S.; Daligou, G.; Moutanabbir, O. Mid-Infrared Detectors and Imagers Integrating All-Group IV Nanowires. *arXiv preprint* **2023**, arXiv:2310.07833.
- (39) Rogers, J. A.; Lagally, M. G.; Nuzzo, R. G. Synthesis, assembly and applications of semiconductor nanomembranes. *Nature* **2011**, *477*, 45–53.

- (40) An, S.; Park, H.; Kim, M. Recent advances in single crystalline narrow band-gap semiconductor nanomembranes and their flexible optoelectronic device applications: Ge, GeSn, InGaAs, and 2D materials. *Journal of Materials Chemistry C* **2023**, 2430–2448.
- (41) Yoon, J.; Lee, S.-M.; Kang, D.; Meitl, M. A.; Bower, C. A.; Rogers, J. A. Heterogeneously integrated optoelectronic devices enabled by micro-transfer printing. *Advanced Optical Materials* **2015**, 3, 1313–1335.
- (42) Linghu, C.; Zhang, S.; Wang, C.; Song, J. Transfer printing techniques for flexible and stretchable inorganic electronics. *npj Flexible Electronics* **2018**, 2, 26.
- (43) Yuan, H.-C.; Wang, G.; Ma, Z.; Roberts, M. M.; Savage, D. E.; Lagally, M. G. Flexible thin-film transistors on biaxial-and uniaxial-strained Si and SiGe membranes. *Semiconductor Science and Technology* **2006**, 22, S72.
- (44) Nam, D.; Sukhdeo, D.; Roy, A.; Balram, K.; Cheng, S.-L.; Huang, K. C.-Y.; Yuan, Z.; Brongersma, M.; Nishi, Y.; Miller, D.; Saraswat, K. Strained germanium thin film membrane on silicon substrate for optoelectronics. *Optics Express* **2011**, 19, 25866–25872.
- (45) Liu, S.-C.; Zhao, D.; Liu, Y.; Yang, H.; Sun, Y.; Ma, Z.; Reuterskiöld-Hedlund, C.; Hammar, M.; Zhou, W. Photonic crystal bandedge membrane lasers on silicon. *Applied Optics* **2017**, 56, H67–H73.
- (46) Zamiri, M.; Anwar, F.; Klein, B. A.; Rasoulof, A.; Dawson, N. M.; Schuler-Sandy, T.; Deneke, C. F.; Ferreira, S. O.; Cavallo, F.; Krishna, S. Antimonide-based membranes synthesis integration and strain engineering. *Proceedings of the National Academy of Sciences* **2017**, 114, E1–E8.
- (47) Pan, W.; Zhang, Z.; Gu, R.; Ma, S.; Faraone, L.; Lei, W. Van der Waals Epitaxy of HgCdTe Thin Films for Flexible Infrared Optoelectronics. *Advanced Materials Interfaces* **2023**, 10, 2201932.

- (48) Tai, Y.-C.; Yeh, P.-L.; An, S.; Cheng, H.-H.; Kim, M.; Chang, G.-E. Strain-free GeSn nanomembranes enabled by transfer-printing techniques for advanced optoelectronic applications. *Nanotechnology* **2020**, *31*, 445301.
- (49) An, S.; Wu, S.; Tan, C. S.; Chang, G.-E.; Gong, X.; Kim, M. Modulation of light absorption in flexible GeSn metal–semiconductor–metal photodetectors by mechanical bending. *Journal of Materials Chemistry C* **2020**, *8*, 13557–13562.
- (50) Atalla, M. R. M.; Assali, S.; Attiaoui, A.; Lemieux-Leduc, C.; Kumar, A.; Abdi, S.; Moutanabbir, O. All-Group IV Transferable Membrane Mid-Infrared Photodetectors. *Advanced Functional Materials* **2021**, *31*, 2006329.
- (51) An, S.; Liao, Y.; Kim, M. Flexible titanium nitride/germanium-tin photodetectors based on sub-bandgap absorption. *ACS Applied Materials & Interfaces* **2021**, *13*, 61396–61403.
- (52) Chen, Q.; Wu, S.; Zhang, L.; Zhou, H.; Fan, W.; Tan, C. S. Transferable single-layer GeSn nanomembrane resonant-cavity-enhanced photodetectors for 2 μm band optical communication and multi-spectral short-wave infrared sensing. *Nanoscale* **2022**, *14*, 7341–7349.
- (53) Menard, E.; Nuzzo, R. G.; Rogers, J. A. Bendable single crystal silicon thin film transistors formed by printing on plastic substrates. *Applied Physics Letters* **2005**, *86*, 093507.
- (54) Liu, Y.; Guo, J.; Zhu, E.; Liao, L.; Lee, S.-J.; Ding, M.; Shakir, I.; Gambin, V.; Huang, Y.; Duan, X. Approaching the Schottky–Mott limit in van der Waals metal–semiconductor junctions. *Nature* **2018**, *557*, 696–700.
- (55) Daligou, G.; Attiaoui, A.; Assali, S.; Del Vecchio, P.; Moutanabbir, O. Radiative carrier lifetime in $\text{Ge}_{1-x}\text{Sn}_x$ midinfrared emitters. *Physical Review Applied* **2023**, *20*, 064001.

- (56) Gupta, S.; Chen, R.; Huang, Y.-C.; Kim, Y.; Sanchez, E.; Harris, J. S.; Saraswat, K. C. Highly Selective Dry Etching of Germanium over Germanium–Tin ($\text{Ge}_{1-x}\text{Sn}_x$): A Novel Route for $\text{Ge}_{1-x}\text{Sn}_x$ Nanostructure Fabrication. *Nano Letters* **2013**, *13*, 3783–3790.
- (57) Bouthillier, É.; Assali, S.; Nicolas, J.; Moutanabbir, O. Decoupling the effects of composition and strain on the vibrational modes of GeSn semiconductors. *Semiconductor Science and Technology* **2020**, *35*, 095006.
- (58) Haq, B.; Kumari, S.; Van Gasse, K.; Zhang, J.; Gocalinska, A.; Pelucchi, E.; Corbett, B.; Roelkens, G. Micro-transfer-printed III-V-on-silicon C-band semiconductor optical amplifiers. *Laser & Photonics Reviews* **2020**, *14*, 1900364.
- (59) Wu, J.-R.; Wu, Y.-H.; Hou, C.-Y.; Wu, M.-L.; Lin, C.-C.; Chen, L.-L. Impact of fluorine treatment on Fermi level depinning for metal/germanium Schottky junctions. *Applied Physics Letters* **2011**, *99*, 253504.
- (60) Keum, H.; Chung, H.-J.; Kim, S. Electrical contact at the interface between silicon and transfer-printed gold films by eutectic joining. *ACS Applied Materials & Interfaces* **2013**, *5*, 6061–6065.
- (61) Mukherjee, S.; Assali, S.; Moutanabbir, O. Atomic Pathways of Solute Segregation in the Vicinity of Nanoscale Defects. *Nano Letters* **2021**, *21*, 9882–9888, PMID: 34797681.
- (62) Assali, S.; Elsayed, M.; Nicolas, J.; Liedke, M. O.; Wagner, A.; Butterling, M.; Krause-Rehberg, R.; Moutanabbir, O. Vacancy complexes in nonequilibrium germanium-tin semiconductors. *Applied Physics Letters* **2019**, *114*, 251907.